

## Research Article

# Stress and Strain State Analysis of Crack Front in Dissimilar Metal Welded Joints with Dual Field of Mechanical Heterogeneity and Residual Stress

Shun Zhang , He Xue , Yubiao Zhang , Kuan Zhao , and Jiaqing Zhang 

*School of Mechanical Engineering, Xi'an University of Science and Technology, Xi'an 710054, China*

Correspondence should be addressed to He Xue; [xuehe@xust.edu.cn](mailto:xuehe@xust.edu.cn)

Received 16 May 2022; Accepted 1 September 2022; Published 17 September 2022

Academic Editor: Leon Cizelj

Copyright © 2022 Shun Zhang et al. This is an open access article distributed under the Creative Commons Attribution License, which permits unrestricted use, distribution, and reproduction in any medium, provided the original work is properly cited.

The micro-mechanical state at the crack front is one of the key factors affecting the stress corrosion cracking (SCC) growth behavior. The mechanical heterogeneity and residual stress in the dissimilar metal welded joint (DMWJ) induce the micro-mechanical state at the crack front to become more complex. The sandwich model and dual-field model of the DMWJ with inner surface axial crack were established in this study. The stress and strain states at the crack front with different crack locations and lengths under the interaction of the mechanical property and the residual stress were investigated. The results show that a more accurate evaluation of stress and strain states can be obtained when using the dual-field model to describe the material mechanical property and residual stress of the DMWJ. The sandwich model overestimates the crack driving force including the stress and strain at the crack front. The tensile stress in the middle of shallow cracks is smaller than that at both ends, while the tensile stress in the middle of deep crack is larger than that at both ends. The variation trend of the tensile stress and normal strain at the crack apex is basically the same as that of the residual stress with the crack depth. However, there is almost no normal plastic strain in the initial stage of crack propagation due to the small residual stress in the initial stage.

## 1. Introduction

Stress corrosion cracking (SCC) is a phenomenon that describes the behavior of crack propagation under the synergistic action of material degradation, mechanics, and an aqueous chemical environment near the micro-area at the crack front. An updated review of the operation of nuclear power plants has demonstrated that the SCC can introduce a considerable hazard to its long-term safety [1]. SCC crack growth rate is an important factor for quantitative evaluation of critical structure lifetime in nuclear power plants. While in the model of SCC crack growth rate calculation, the micro-mechanical state at the crack front is one of the key factors that determine the SCC growth rate [2-4]. Moreover, this micro-mechanical state tends to exhibit variability and complexity during the service due to the mechanical heterogeneity and the residual stress in the actual dissimilar metal welded joint (DMWJ) at the safety-end of the nuclear power plant. Therefore, it is difficult to predict the crack

propagation behavior of SCC in DMWJ, which is a weak link in the whole research field of the structural integrity of the nuclear power plant. A more accurate SCC growth behavior can be obtained by studying the mechanical field distribution at the crack front under the interaction of mechanical heterogeneity and residual stress, which reduces the overly conservative safety assessment in engineering, and then the operation and life extension scheme are improved. Hence, the study about the interaction of mechanical heterogeneity and residual stress may have promising beneficial effects on the safe and stable operation of the nuclear power plant.

The bi-material model with welded metal and base metal is usually used in the traditional research on fracture behavior of the material interface. These models are generally called sandwich models which have a sudden change of mechanical properties at the material interface [5, 6]. As a result, the stress-strain field around the tip of the interface crack has a sudden cliff-typed change under the sandwich model [7]. However, an earlier study showed that the

interfaces of two materials in the DMWJ are not strictly differentiated, and especially noteworthy is that the mechanical properties change continuously at the material interface between two materials [8, 9]. Therefore, the sandwich model may not meet the requirements for a more accurate analysis of the SCC crack front stress state of the DMWJ. Meanwhile, the SCC behavior is also closely related to the residual stress [10, 11]. Nam et al. [12] confirmed that residual stress acts as a dominant factor in the initiation and growth of SCC by investigating an artificial SCC which is made in STS 304. Surface and subsurface residual stress distribution was assessed by Rhouma et al. [13] using X-ray diffraction (XRD). The result shows that the tensile residual stress directionality and level play a major role in the corrosion micro-crack initiation and in the resulting micro-crack network morphology. However, under the interaction of mechanical heterogeneity and the residual stress, stress and strain states at axial direction SCC crack front with different crack locations and depths in the DMWJ have not been investigated and understood. Rapid advances in finite element software make it an effective tool for crack analysis [14–17].

In this research, to characterize the mechanical properties and the residual stress of the DMWJ, the user-defined field (USDFLD) was used to establish the non-uniform field of mechanical properties of materials, and the predefined stress field method was used to set the residual stress field in the finite element software. Then, the dual-field model of the DMWJ with inner surface axial crack was established. The mechanical field of the crack front with different crack locations and lengths under the interaction of the mechanical properties and the residual stress was investigated.

## 2. Numerical Simulation and Experiments

**2.1. Experiments.** The DMWJ sample provided by the Institute of Metal Research, Chinese Academy of Sciences, is used in this research. Its sampling schematic diagram in the typical AP1000 pressurized water reactor (PWR) nuclear power plant is shown in Figure 1. The ferritic low alloy steel (A508) and austenitic stainless steel (316L) are used for the nozzle of the nuclear pressure vessel and safety-end pipe, respectively. The nickel-base alloy (52M) is used for the welded metal, including 52Mb which is welded by the buttering technique.

In this study, to obtain the more detailed distribution of material mechanical properties of the DMWJ, the distribution of Vickers hardness was measured on the sample, which is shown in Figure 2. It shows that the hardness near the heat affected zone (HAZ) has increased significantly.

**2.2. FEM Model.** To study the effect of different crack locations and crack lengths on the stress and strain around the crack front, 11 crack locations have been selected. The simplified model of the DMWJ has ignored the welding slope of buttering layer and A508, where the geometric size of the model is  $60 \times 30 \times 10$  mm, as shown in Figure 3. Crack-1 is located in the centre of 52M of the weld, and the crack

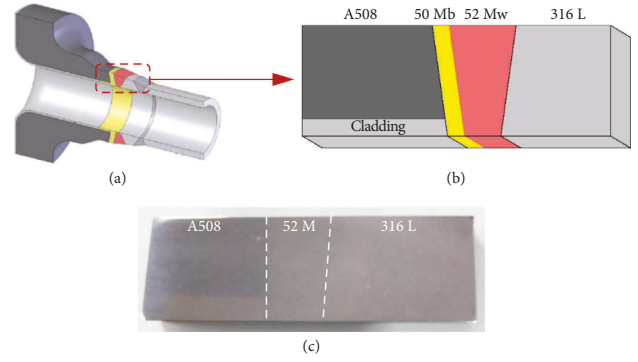


FIGURE 1: DMWJ at safety end in PWR nuclear power plant. (a) Safety end and sampling position. (b) Three-dimensional geometrical model. (c) DMWJ sample.

size is  $5 \times 21$  mm ( $a \times 2c$ ). When it expands to 25 mm along the Y direction, the crack size includes 9 different lengths with equal intervals (2.5 mm), and the shape of the crack front remains unchanged ( $2c = 21$  mm). The centre of Crack-10 and Crack-11 is located at the interface of A508-52M and 52M-316L, and both crack sizes are  $5 \times 21$  mm. The three-dimensional finite element model used about 18414 20-node quadratic brick and reduced integration (C3D20R) elements. The meshes around the crack front were refined in spider mesh with 7488 C3D20R elements. The three-dimensional finite element model and locally refined crack front meshes are shown in Figure 4.

The sandwich model and dual-field model of the DMWJ were established to compare the stress and strain states at the crack front in this study. The stress-strain relation of the safety-end welded structure materials conforms to the Ramberg–Osgood (RO) equation, namely,

$$\frac{\varepsilon}{\varepsilon_0} = \frac{\sigma}{\sigma_0} + \alpha \left( \frac{\sigma}{\sigma_0} \right)^n, \quad (1)$$

where  $\sigma_0$  is the yield strength,  $\varepsilon_0$  is the yield strain,  $\alpha$  is the RO coefficient, and  $n$  is the work hardening exponent. In general, all parameters are consistent except the yield strength and the work hardening exponent in most studies of crack propagation in welded joints [18, 19]. Thus, Young's modulus  $E$ , Poisson's ratio  $\nu$ , and RO coefficient  $\alpha$  of the DMWJ are, respectively, constant (202,000 MPa, 0.3, and 1) in this study. Based on the relationship between Vickers hardness and the yield strength of welded joints [20], the yield strength could be obtained according to the Vickers hardness HV distribution of DMWJ in Figure 2. Figure 5 shows the yield strength distribution of the dual-field model and sandwich model. In the sandwich model, the yield strength of A508, 52M, and 316L is set as 535 MPa, 634 MPa, and 358 MPa, respectively. In the dual-field model, the yield strength distribution is shown in Figure 5, which was established by the user-defined field subroutine (USDFLD) in ABAQUS. The work hardening exponent  $n$  can be obtained according to the yield strength [21].

$$n = \frac{1}{\kappa \ln(1390/\sigma_0)}, \quad (2)$$

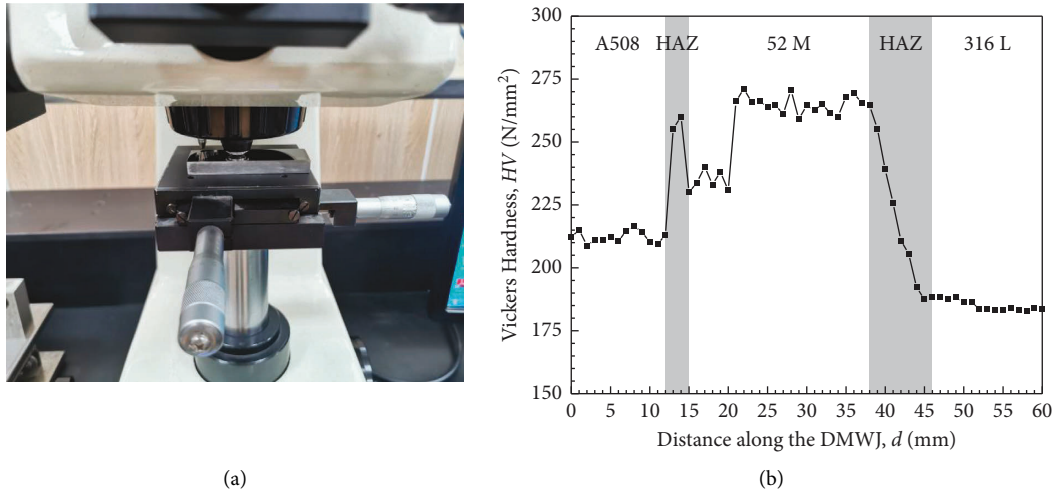


FIGURE 2: Vickers hardness experiment. (a) Experimental process. (b) Vickers hardness  $HV$  distribution of the DMWJ sample.

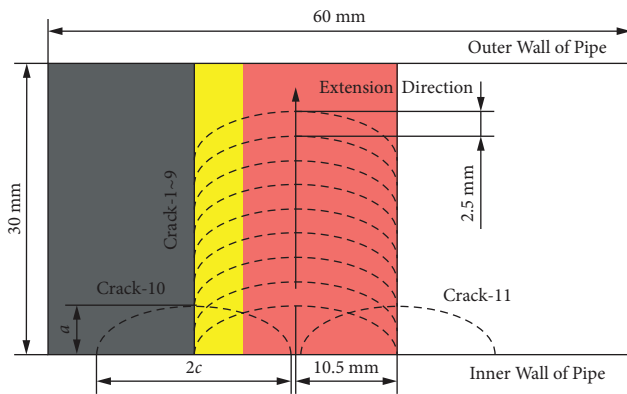


FIGURE 3: Sketch map of crack locations in the DMWJ sample.

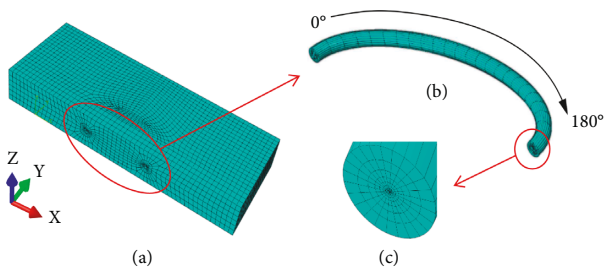


FIGURE 4: Finite element mesh model. (a) Global model. (b) Refined crack front meshes. (c) Front surface of crack front meshes.

where  $k=0.163$ . Also, the continuous change of the yield strength along the  $X$  direction in the finite element model realized by the USDFLD is shown in Figure 6.

In the dual-field model, according to the residual stress distribution of dissimilar metal welded joints at the safety end of nuclear power [22], the residual stress distribution along the  $Y$  direction added in this study is shown in Figure 7. The residual stress was applied by the predefined stress field method in this study. Figure 8 shows the continuous distribution of residual stress in the finite element model, which is consistent with the distribution curve of residual stress shown in Figure 7. Most SCC tests are

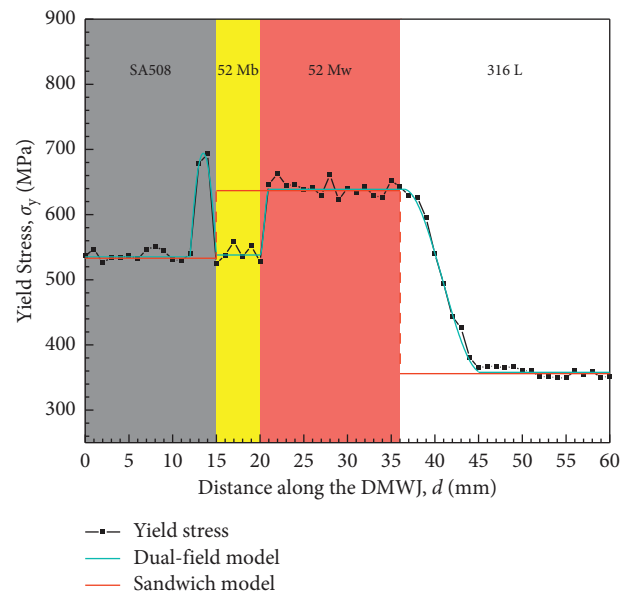


FIGURE 5: Yield strength distribution of sandwich model and dual-field model of the DMWJ.

performed on specimens under constant load [23, 24], and the uniform stress load was used in the sandwich model. Its value is 204 MPa, which is the average value of the residual stress in the dual-field model.

To sum up, two models of the DMWJ for investigating the stress and strain states at the crack front were established in this study. One is a sandwich model with strictly differentiated material interfaces, in which the residual stress is applied with a constant load. The other is a dual-field model in which mechanical properties change continuously at the interface, and a residual stress field is applied.

### 3. Results and Discussion

**3.1. Different Crack Locations.**  $20\ \mu\text{m}$  in front of the crack tip can be used as the characteristic point [2]. Therefore, this

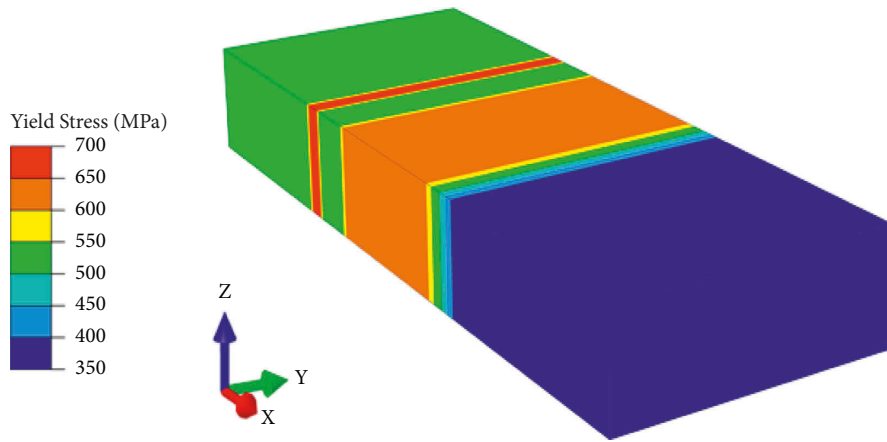


FIGURE 6: Yield strength contour distribution in the dual-field model.

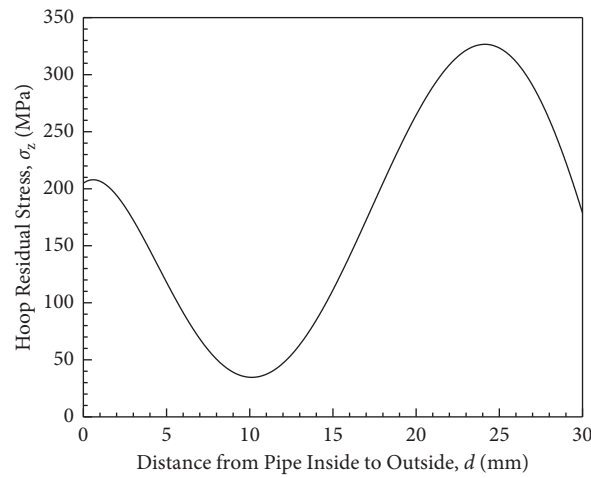


FIGURE 7: Hoop (Z-direction) residual stress distribution along the Y direction of the DMWJ.

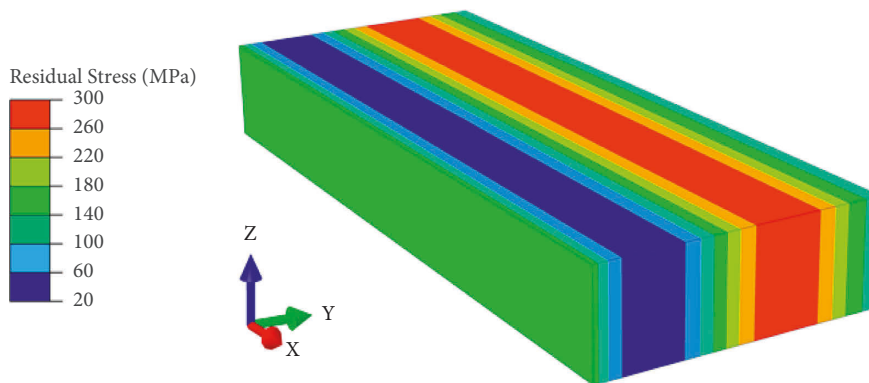


FIGURE 8: Residual stress contour distribution in the dual-field model.

point is selected as the characteristic point to analyze the stress and strain states at the crack front in this study. Figure 9 shows the tensile stress at the crack front along crack angle of Crack-1, Crack-10, and Crack-11. As shown in Figure 9(a), the tensile stress has a sudden cliff-typed change at the interface of A508 and 52M because of the sudden change in the yield strength of the bi-materials at the

interface in the sandwich model. In contrast, the tensile stress increases at the HAZ in the dual-field model due to the high strength in the HAZ of A508. Figure 9(b) illustrates that the distribution of tensile stress at the crack front along the crack angle is smooth and symmetrical due to the constant yield strength of the whole 52M in the sandwich model. Furthermore, the maximum value is near the crack apex

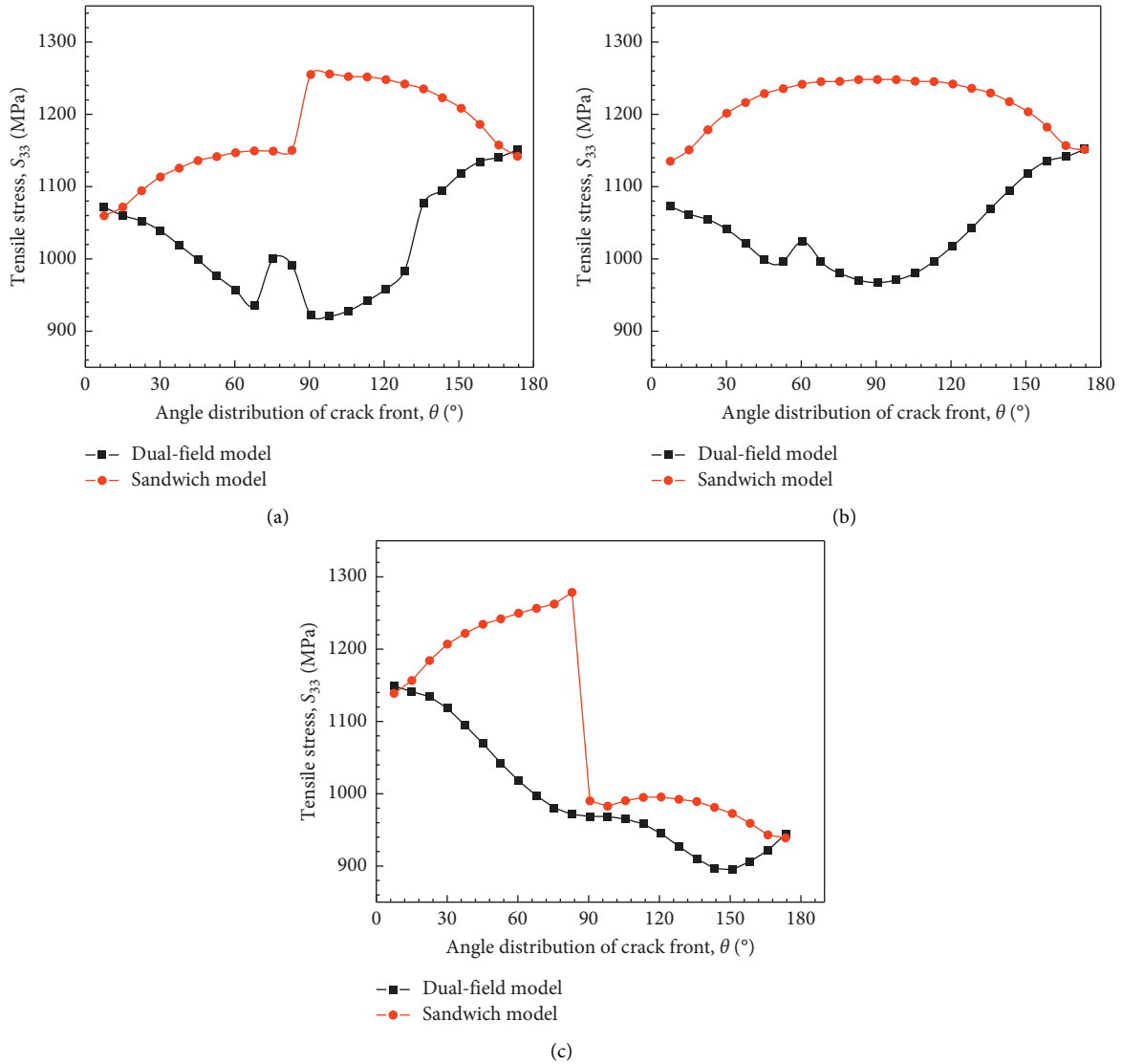


FIGURE 9: Distribution of tensile stress along crack front with crack angle. (a) Crack-10. (b) Crack-1. (c) Crack-11.

( $\theta = 90^\circ$ ), whereas the tensile stress distribution of the dual-field model is opposite to that of the sandwich model, there is a maximum near the interface of 52 Mb and 52 Mw. This maximum is the local maximum, which is compared to the material in the left and right regions of the interface (52 Mb and 52 Mw). Figure 9(c) shows that the mutation of tensile stress is larger than that of Crack-10 due to the larger difference in the yield strength between 52M and 316L in the sandwich model. In the dual-field model, the tensile stress decreases gently with the increase of the crack angle because of the reduction in the yield strength, and the minimum value is near  $\theta = 150^\circ$ . Comparing Figures 9(a)–9(c), it can be found that compared with the dual-field model, the tensile stress at the crack front has an apparent mutation at the material interface in the sandwich model, which is consistent with the results of previous studies [25]. The tensile stress at the crack front is overestimated than that in the dual-field model.

The relationships between the normal plastic strain at the crack front and the crack angle of Crack-10, Crack-1, and

Crack-11 are depicted in Figure 10. It can be seen from Figure 10(a) that the sandwich model has a sudden cliff-typed change at the interface between A508 and 52M, which is similar to tensile stress variation, but the trend is opposite to tensile stress. Moreover, in the dual-field model, the normal plastic strain in the HAZ of A508 decreases due to the high yield strength in this zone, and the minimum value close to zero is located in the HAZ. Figure 10(b) shows that the normal plastic strain distribution at the crack front is relatively smooth and symmetrical due to the homogeneous material used in the whole 52M welding material of the sandwich model. However, the normal plastic strain of the dual-field model at the crack front of 52 Mb increases sharply, even surpasses that of the sandwich model, because the yield strength of 52 Mb in the dual-field model is smaller than that of 52 Mw, and the maximum value is located at the leftmost end of the crack. Figure 10(c) shows that the normal plastic strain mutation of Crack-11 in the sandwich model is larger than that of Crack-10, while the normal plastic strain

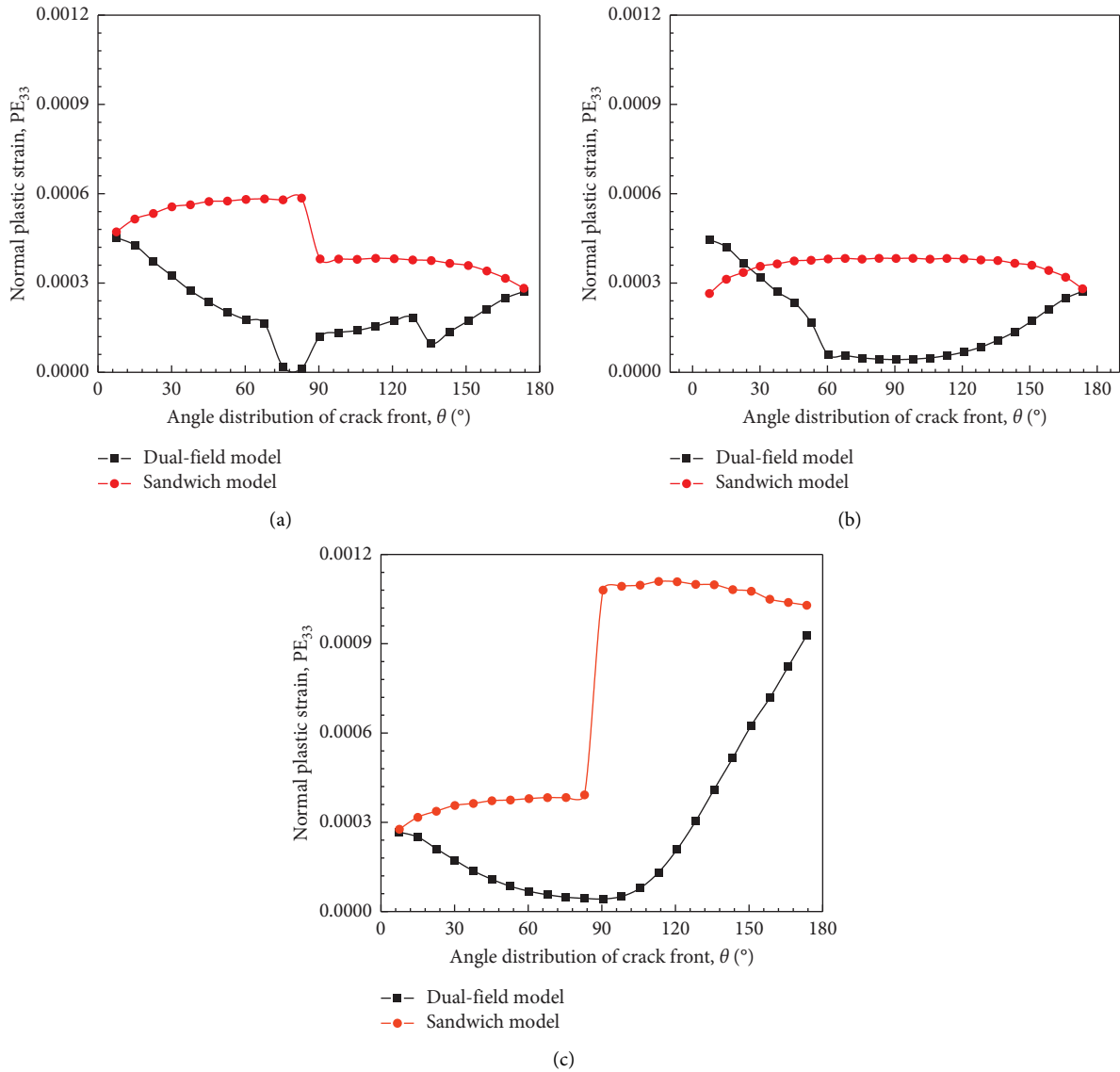


FIGURE 10: Distribution of normal plastic strain along crack front with crack angle. (a) Crack-10. (b) Crack-1. (c) Crack-11.

in the dual-field model changes continuously, and the normal plastic strain in 316L is greater than that in 52M. The analysis combined with Figures 10(a)–10(c) indicates that the sandwich model overestimates the normal plastic strain at crack fronts of cracks generally compared with the dual-field model.

**3.2. Different Crack Depths.** Figure 11 shows the tensile stress distribution at the crack front along the crack angle of different crack depths. Cracks-1~3 are in the stage where the residual stress gradually decreases along the crack growth direction, and Cracks-4~9 are in the stage of gradually increasing residual stress. It can be seen from Figure 11(a) that at the initial stage of crack propagation (Cracks-1~3), the overall tensile stress decreases as the increase of crack length, and the tensile stress at both ends of Cracks-1~3 is greater than that at the middle. Combined with Figures 11(a) and 11(b), in other cracks (Cracks-4~9), the overall tensile stress

increases with the increase of crack length, and the tensile stress in the middle of the crack is larger than that at both ends. Combining Figures 3 and 7, we can find that the residual stress at the crack front changes with the crack growth. Cracks-1~3 (shallow cracks) are in the stage where the residual stress gradually decreases along the crack growth direction, so the tensile stress in the deepest part of the crack ( $\theta = 90^\circ$ ) is the smallest. However, Cracks-4~9 (deep surface crack) are in the stage of gradually increasing residual stress, so the tensile stress in the deepest part of the crack ( $\theta = 90^\circ$ ) is the largest. Therefore, under the dual-field interaction, the tensile stress in the middle of shallow cracks is smaller than that at both ends obviously, while the tensile stress in the middle of deep surface crack is larger than that at both ends. Furthermore, it can be inferred that in the process of crack growth, due to the variable driving forces under the influence of the residual stress and mechanical properties, its shape may not be a simple regular ellipse.

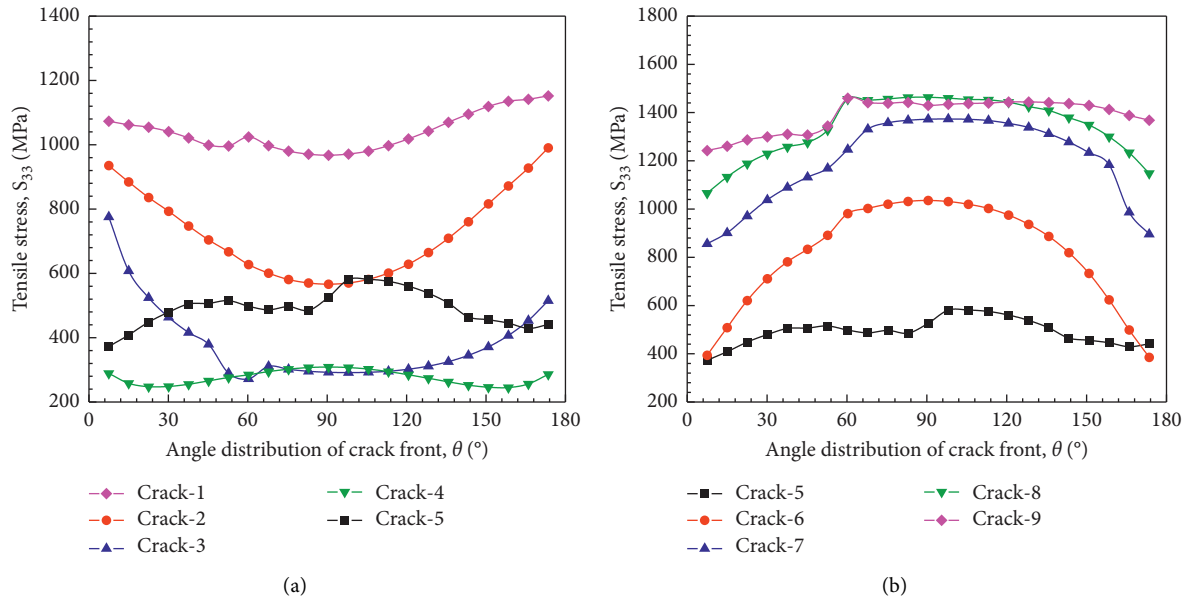


FIGURE 11: Distribution of tensile stress along crack front with crack angle. (a) Cracks-1~5. (b) Cracks-5~9.

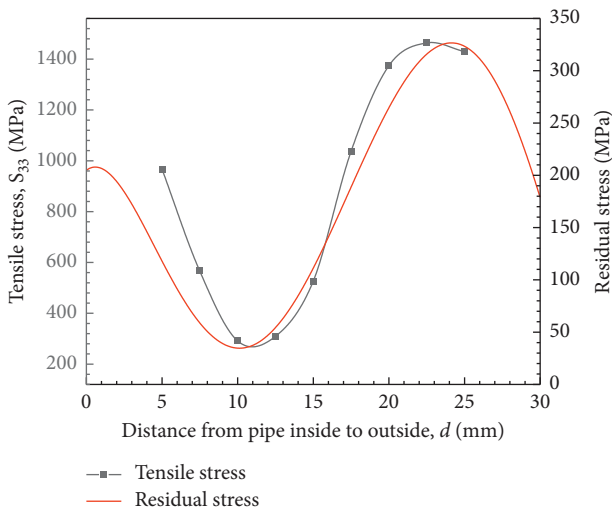


FIGURE 12: Tensile stress at crack apex ( $\theta = 90^\circ$ ) with crack length.

To further study the relationship between the tensile stress at the crack front and residual stress, the crack apex ( $\theta = 90^\circ$ ) is taken as a representative to plot the relationship with the crack length, as shown in Figure 12. It can be seen that the tensile stress at the crack apex firstly decreases and then increases and finally decreases with the increase of the crack length, which is consistent with the distribution of residual stress. However, the minimum value of tensile stress lags behind the minimum value of residual stress and the maximum value advances to the maximum value of residual stress. This is because the propagation of the crack breaks the original self-balanced state of the residual stress, and the residual stress is redistributed. Therefore, the variation trend of the tensile stress at the crack front does not completely coincide with the original distribution of residual stress. This phenomenon was studied in detail in [14]. This figure can

better describe the effect on tensile stress at the crack front of non-uniform residual stress during the crack growth. In other words, the tensile stress at the front of the crack changes with different residual stress in corresponding crack lengths. Therefore, the tensile stress at the crack front is affected not only by the geometry of the crack length but also by the redistribution of residual stress.

Figure 13 illustrates the normal plastic strain distribution at the crack front with different crack depths. It can be seen that in the initial stage of crack propagation (Cracks-1~2), the overall normal plastic strain decreases with the increase of crack length, and the normal plastic strain at both ends of Cracks-1~2 is greater than that in the middle. However, it can be obviously found that the normal plastic strain of Cracks-3~5 is close to zero. There is almost no plastic strain because the tensile stress at the crack front of Cracks-3~5 is relatively small in Figure 12. From Crack-6, the normal plastic strain at the crack front increases with the increase of the crack depths. Also, due to the smaller yield strength of 52 Mb than 52 Mw, the normal plastic strain at the crack front is greater than that of 52 Mw, and the maximum values are all in 52 Mb.

Similar to Figure 12, the crack apex ( $\theta = 90^\circ$ ) is taken as a representative to plot the relationship between the normal strain (including the normal plastic strain) and residual stress with the crack length. It can be seen from Figure 14 that the normal strain at the crack apex decreases first and then increases and finally decreases with the increase of the crack length, which is consistent with the distribution of the tensile stress at crack apex in Figure 12. In other words, the variation trend of the normal strain at the crack front with the crack length is basically consistent with that of the residual stress. However, the normal plastic strain at the crack apex is close to zero in Cracks-2~5. According to the distribution of the tensile stress at crack apex in Figure 12, the tensile stress at crack apex of Cracks-2~5 is basically less

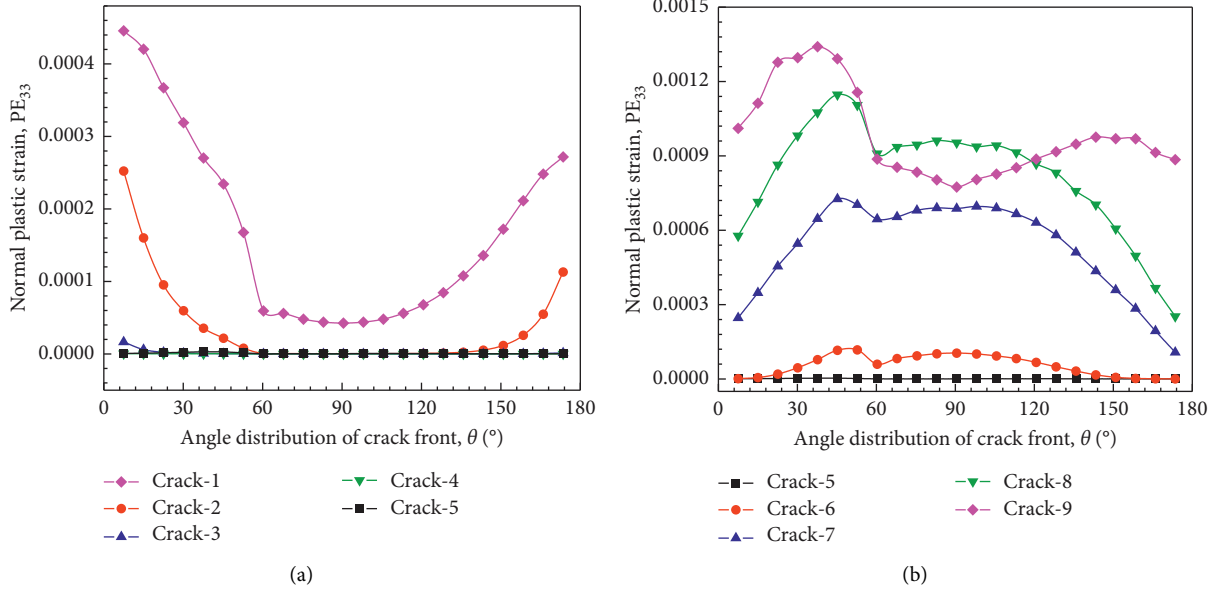


FIGURE 13: Distribution of normal plastic strain along crack front with crack angle. (a) Cracks-1~5. (b) Cracks-5~9.

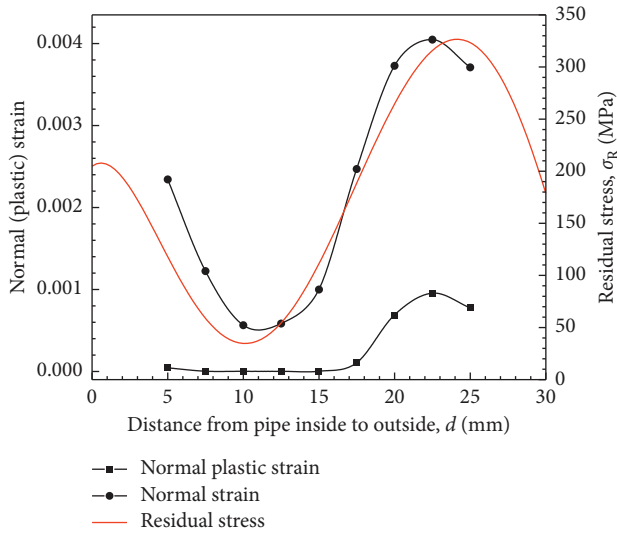


FIGURE 14: Strain at crack apex ( $\theta = 90^\circ$ ) with crack length.

than the yield stress of 52 Mw (634 MPa). Therefore, the plastic deformation near the crack front is very small and the elastic strain is dominant. Therefore, the change of normal plastic strain at the crack apex with the crack length is not consistent with the distribution of residual stress.

Above all, the tensile stress in the middle of the shallow crack is significantly smaller than that of the two ends under the interaction of the inhomogeneous field of material mechanical properties and the residual stress field, while the tensile stress in the middle of the deep crack is relatively uniform and larger than that of the two ends. The variation trend of the tensile stress at the crack apex with the crack length is basically consistent with the residual stress distribution. Similarly, the normal strain variation trend at the crack apex is consistent with tensile stress, but the normal

plastic strain is not consistent with the distribution of residual stress.

## 4. Conclusions

- (1) Compared with the traditional sandwich model, a more accurate evaluation of stress and strain states can be obtained when using the dual-field model to describe the mechanical heterogeneity and residual stress of the DMWJ. The sandwich model overestimates the crack driving force including the stress and strain at the crack front.
- (2) When the inner surface axial crack propagates to the interface of A508 and 52M, the tensile stress at the crack front in HAZ of A508 increases, but the normal plastic strain decreases. When the inner surface axial crack propagates to the interface of 316L and 52M, the tensile stress at the crack front in 316L is less than that in 52M, but the normal plastic strain is greater than that in 52M, and the stress and strain change gently due to the smooth transition of material properties in HAZ of 316L.
- (3) The tensile stress in the middle of shallow surface cracks is smaller than that at both ends obviously, while the tensile stress in the middle of deep surface crack is larger than that at both ends. The variation trend of the tensile stress at the crack apex is basically the same as that of the residual stress with the crack depth, but the position of the maximum and minimum of the two is different due to the redistribution of the residual stress.
- (4) The normal strain distribution at the crack apex with the crack depths is the same as the tensile stress. However, there is almost no normal plastic strain in

the initial stage of crack propagation because the tensile stress does not reach the yield strength.

For the purpose of structural integrity analyses, many efforts have been made to reduce unnecessary conservatism in the guidance of engineering practices. Using the dual-field model of mechanical heterogeneity and residual stress may help to achieve this purpose by providing a better understanding of the prediction of the crack driving force.

### Data Availability

The data of interaction of mechanical heterogeneity and residual stress on mechanical field at the crack front used to support the findings of this study are included within the article.

### Conflicts of Interest

The authors declare that they have no conflicts of interest.

### Acknowledgments

This study was supported by the National Natural Science Foundation of China (52075434) and Natural Science Foundation of Shaanxi Provincial Department of Education (2021KW-36 and 2021JM-389).

### References

- [1] P. L. Andresen, "A brief history of environmental cracking in hot water," *Corrosion*, vol. 75, no. 3, pp. 240–253, 2018.
- [2] H. Xue, Z. Li, Z. Lu, and S. Tetsuo, "The effect of a single tensile overload on stress corrosion cracking growth of stainless steel in a light water reactor environment," *Nuclear Engineering and Design*, vol. 241, pp. 731–738, 2011.
- [3] Z. Li, Y. Lu, and X. Wang, "Modeling of stress corrosion cracking growth rates for key structural materials of nuclear power plant," *Journal of Materials Science*, vol. 55, no. 2, pp. 439–463, 2020.
- [4] Q. J. Peng, J. Kwon, and T. Shoji, "Development of a fundamental crack tip strain rate equation and its application to quantitative prediction of stress corrosion cracking of stainless steels in high temperature oxygenated water," *Journal of Nuclear Materials*, vol. 324, no. 1, pp. 52–61, 2004.
- [5] K. Fan, G. Z. Wang, F. Z. Xuan, and S. Tu, "Effects of work hardening mismatch on fracture resistance behavior of bi-material interface regions," *Materials & Design*, vol. 68, pp. 186–194, 2015.
- [6] U. Zerbst, R. A. Ainsworth, H. T. Beier et al., "Review on fracture and crack propagation in weldments-A fracture mechanics perspective," *Engineering Fracture Mechanics*, vol. 132, pp. 200–276, 2014.
- [7] H. Xue, K. Ogawa, and T. Shoji, "Effect of welded mechanical heterogeneity on local stress and strain ahead of stationary and growing crack tips," *Nuclear Engineering and Design*, vol. 239, no. 4, pp. 628–640, 2009.
- [8] H. T. Wang, G. Z. Wang, F. Z. Xuan, C. Liu, and S. Tu, "Local mechanical properties of a dissimilar metal welded joint in nuclear powersystems," *Materials Science and Engineering A*, vol. 568, pp. 108–117, 2013.
- [9] M. Akbari and P. Asadi, "Dissimilar friction stir lap welding of aluminum to brass: modeling of material mixing using coupled Eulerian–Lagrangian method with experimental verifications," *Proceedings of the Institution of Mechanical Engineers-Part L: Journal of Materials: Design and Applications*, vol. 234, no. 8, pp. 1117–1128, 2020.
- [10] X. He, C. Yinghao, L. Gangbo, and W. Shuai, "Crack growth driving force at tip of stress corrosion cracking in nuclear structural materials at initial stage," *Rare Metal Materials and Engineering*, vol. 47, no. 8, pp. 2365–2370, 2018.
- [11] P. J. Withers, "Residual stress and its role in failure," *Reports on Progress in Physics*, vol. 70, no. 12, pp. 2211–2264, 2007.
- [12] J. Y. Nam, D. h Seo, S. y Lee, W. K. Hwang, and B. Y. Lee, "The effect of residual stress on the SCC using ANSYS," *Procedia Engineering*, vol. 10, pp. 2609–2614, 2011.
- [13] A. B. Rhouma, N. Sidhom, K. Makhoulouf, H. Sidhom, C. Braham, and G. Gonzalez, "Effect of machining processes on the residual stress distribution heterogeneities and their consequences on the stress corrosion cracking resistance of AISI 316L SS in chloride medium," *International Journal of Advanced Manufacturing Technology*, vol. 105, no. 1–4, pp. 1699–1711, 2019.
- [14] Y. Zhang, H. Xue, S. Zhang et al., "Interaction of mechanical heterogeneity and residual stress on mechanical field at crack tips in DMWJs," *Science and Technology of Nuclear Installations*, vol. 2022, pp. 1–11, 2022.
- [15] D. N. L. Alves, J. G. Almeida, and M. C. Rodrigues, "Experimental and numerical investigation of crack growth behavior in a dissimilar welded joint," *Theoretical and Applied Fracture Mechanics*, vol. 109, Article ID 102697, 2020.
- [16] H. T. Wang, G. Z. Wang, F. Z. Xuan, and S. Tu, "Numerical investigation of ductile crack growth behavior in a dissimilar metal welded joint," *Nuclear Engineering and Design*, vol. 241, no. 8, pp. 3234–3243, 2011.
- [17] R. Guo, H. Xue, and X. Gong, "Influence of residual stress and heterogeneity on mechanical field at crack tips in safety end of nuclear power plant," *Procedia Structural Integrity*, vol. 13, pp. 2202–2209, 2018.
- [18] A. M. Sisan and A. Motarjemi, "The effect of strength mismatch and residual stress in ECA of girth welds with internal circumferential cracks," *ASME Pressure Vessels and Piping Conference*, vol. 6, pp. 1807–1813, 2009.
- [19] Y. Takashima, Y. S. Yamada, T. Handa, S. Igi, K. Oi, and F. Minami, "Numerical analysis of strength mismatch effect on stress field in Charpy specimen," *Welding in the World*, vol. 59, no. 3, pp. 433–441, 2015.
- [20] Y. Peng, C. Wu, J. Gan, and J. Dong, "Characterization of heterogeneous constitutive relationship of the welded joint based on the stress-hardness relationship using micro-hardness tests," *Construction and Building Materials*, vol. 202, pp. 37–45, 2019.
- [21] Y. Ueda, Y. W. Shi, and S. Y. Sun, "Effects of crack depth and strength mismatching on the relation between J-integral and CTOD for welded tensile specimens," *Transactions of JWRI*, vol. 26, no. 2, pp. 133–140, 1997.
- [22] I. Muroya, Y. Iwamoto, N. Ogawa, H. Kiminobu, and O. Kazuo, "Residual stress evaluation of dissimilar weld joint using reactor vessel outlet nozzle mock-up model (report-1)," *ASME Pressure Vessels and Piping Conference*, vol. 48296, pp. 613–623, 2008.
- [23] R. Zhu, J. Wang, Z. Zhang, and E. H. Han, "Stress corrosion cracking of fusion boundary for 316L/52M dissimilar metal weld joints in borated and lithiated high

- temperature water,” *Corrosion Science*, vol. 120, pp. 219–230, 2017.
- [24] P. I. Andresen and M. M. Mom, “SCC of stainless steels and Ni alloys in high temperature water,” *Corrosion*, vol. 2007, p. 7612, 2007.
- [25] H. Xue, Y. Sun, S. Zhang et al., “A numerical approach to analyze detail mechanical characteristic at the crack tip of SCC in dissimilar metal welded joints,” *Advances in Materials Science and Engineering*, vol. 2021, Article ID 8429051, 12 pages, 2021.